J Infrared Milli Terahz Waves
DOI 10.1007/s10762-013-9985-3

Elimination of Fresnel Reflection Boundary Effects and Beam Steering in Pulsed Terahertz Computed Tomography

Suman Mukherjee · John Federici · Paulo Lopes · Miguel Cabral

Received: 4 February 2013 / Accepted: 23 May 2013

Abstract For the past few decades there has been tremendous innovation and development of Terahertz (THz) science and imaging. In particular, the technique of 3-D computed tomography has been adapted from the X-Ray to the THz range. However, the finite refractive index of materials in the THz range can severally refract probing THz beams during the acquisition of tomography data. Due to Fresnel reflection power losses at the boundaries as well as steering of the THz beam through the sample, refractive effects lead to anomalously high local attenuation coefficients near the material boundaries of a reconstructed image. These boundary phenomena can dominate the reconstructed THz-CT images making it difficult to distinguish structural defect(s) inside the material. In this paper an algorithm has been developed to remove the effects of refraction in THz-CT reconstructed images. The algorithm is successfully implemented on cylindrical shaped objects.

Keywords Terahertz · Computed tomography (CT) · Non-destructive evaluation (NDE) · Natural cork · Structural defect

1 Introduction

Terahertz Time-Domain Spectroscopy (THz-TDS) and imaging is a coherent measurement technology which is based on the measurement of a THz pulse in the time-domain. The Fourier transform of the pulse waveform gives measurement of both the frequency

S. Mukherjee (✉) · J. Federici
Department of Physics, New Jersey Institute of Technology, Newark, NJ 07102, USA
e-mail: sm243@njit.edu

J. Federici
e-mail: federici@njit.edu

P. Lopes · M. Cabral
Research & Development, Amorim & Irmãos, S.A., Porto, Portugal

P. Lopes
e-mail: pdlopes.ai@amorim.com

M. Cabral
e-mail: mcabral.ai@amorim.com

Published online: 12 June 2013

dependent phase as well as amplitude of the THz pulse. Pulsed Terahertz (THz) imaging was first proposed by Hu and Nuss in 1995 [1].

Time-domain THz waves provide temporal and spectroscopic information that enables development of various three-dimensional (3D) terahertz tomography imaging modalities [2, 3]. The interaction between a coherent THz pulse and an object provides rich information about the object under study; therefore, three-dimensional terahertz imaging is a very useful tool to inspect or characterize several types of objects. THz tomography was first demonstrated in 1997 by Mittleman et al. [4]. X-Ray computed tomography (CT) is an excellent methodology to measure the 3D cross sectional images of materials and much of the same methodology has been adapted in the THz and millimeter wave regions. For example, a variety of instrumentation hardware have been used for THz tomography systems including all-electronic 3D computed THz tomography operating in the 230–320 GHz frequency range of [5], 3D THz imaging using single cycle THz pulses [6], continuous wave (CW) terahertz tomography with phase unwrapping [7], THz-CT using CW a gas laser operating at 2.25 THz [8], and THz optical coherence tomography based on quantum cascade lasers [9]. Applications of THz computed tomography include 3D images of turkey [10] and human bones [11] as well as foam material [12] with various defects and voids. Using foam samples with voids as well as a wooden doll as test objects, Recur et al. [13] compared different THz-CT image reconstruction methods. Maryelle *et al.* investigated 3D THz-CT of dried human bones [11]. The authors generated THz-CT images of lumbar vertebra, a coxal bone, and a skull and made direct comparison with X-Ray 3D-CT images. Although THz has lower resolution than X-Ray, it was evident from their measurement that THz-3D-CT images can distinguish between compact bones and spongy bones.

Due to its non-ionizing nature THz imaging has been used widely as for non-destructive evaluation (NDE) of different materials. Non-destructive evaluation (NDE) of natural cork, for example, has been demonstrated [14] by imaging the internal crack, voids, and grain structure of natural cork samples. For NDE of materials for which the internal structure is not uniform, artifacts in the reconstructed image can mask the subtle but important contrast in a sample's internal structure. In our previous study of internal defects in natural cork, [15] pulsed THz-CT was used to reconstruct the cork's internal structure. However, the strong boundary artifact made resolution of the mass density variations, cracks, voids, and channels of the cork structure difficult to discern. For natural cork, it is the internal structure which is thought to determine the gas diffusion properties of natural cork which are essential for the functionality of natural cork as barrier to gas and liquid diffusion [16, 17].

Clearly, the vastly different spatial scales of X-Rays and Terahertz radiation suggest that the reconstruction methodologies which are routinely employed in the X-Ray range may not be optimal in the THz range. X-Rays, due to their nature, travel through the target material in almost straight lines without much refraction. Due to the refractive index change at material boundaries, THz waves are susceptible to refraction as well as loss of signal due to Fresnel reflection from boundaries. Due to the enhanced loss of THz power at a boundary due to both Fresnel reflection losses as well as refractive losses, reconstructed THz–CT images exhibit enhanced attenuation at the boundaries and also a distortion of the boundary shapes. Examples of the boundary effect can be seen in many papers on THz CT imaging [3, 4, 18–20]. Only in the case of a low refractive index contrast material [8, 9, 21, 22] can the refractive and reflective effects be ignored in the image reconstruction.

Other examples of adapting X-ray CT to the THz range include incorporating the Gaussian beam properties in the image reconstruction process to improve the quality of the reconstructed images [23]. In that work the authors simulated Gaussian beam properties. When the beam properties are included, the reconstructed images show differences

compared to standard reconstructed images. A small number of papers have studied boundary artifact phenomenon and have tried to remove the prominent boundary effect phenomena by different methodologies. E. Abraham *et al.* [24] introduce a multi-peak averaging method to eliminate boundary effects due to refraction losses of the THz beam inside the material. As the THz beam propagates through the material, it suffers refraction inside the material and thus produces multiple peaks - instead of a single peak - when it passes through a material. In [24] a time delay from a particular peak is used to generate tomographic images. However, the presence of multiple peaks makes it difficult to choose the correct peak for time delay measurement. By averaging several of the peaks and considering the time delay of that averaged peak, the boundary effect can be reduced. In applying this technique to 3D THz-CT images of a Teflon cylinder (refractive index 1.37) with a hole on it, the effect of the boundaries is reduced, but the visibility of boundaries are still artificially enhanced in the reconstructed image.

In the present paper, we show that by correcting for the two most dominant phenomena (i.e. steering of the THz beam and Fresnel reflection) prior to image reconstruction, the boundary effect can be essentially eliminated. While an accurate reconstruction of an object with arbitrary shape and composition by THz CT is problematic due to refraction artifacts, THz CT can still be an effective NDE tool if the general shape of an object under test is known. If the shape and refractive index of a 'standardized' object were known *a-priori*, then in principle the effects of Fresnel reflection and refraction could be removed from CT projection data prior to applying an inverse Radon transformation to reconstruct the image. By removing the boundary artifacts, the discrimination of internal structure of a test object compared to the ideal 'standardized' object could be greatly improved. For the specific example of NDE of cylindrically shaped natural cork stoppers, the outer size and shape of each sample is essentially the same from sample to sample. Removing the boundary artifacts enables a more detailed reconstruction of each sample's internal structure which is so critical to the functionary of the stoppers with regards to their gas and liquid diffusion properties.

In this paper, a methodology is introduced for removing boundary artifacts in THz CT imaging for cylindrically shaped objects. In Section 2, the experimental procedure and manifestation of the boundary artifact in the reconstructed image are described. In Section 3, the mathematical algorithms for correcting CT projections prior to image reconstruction are described. In Section 4, the correction algorithm is applied to a series of plastic rods and natural cork. The major conclusions are summarized in Section 5.

2 Experimental Procedure and Boundary Artifacts

While the longer term goal is to apply the developed algorithms to NDE of cylindrical cork stoppers, the non-homogeneous internal structure of cork and significant sample to sample variations clearly precludes natural cork as a model material for the development of correction algorithms. In order to study the boundary effect and develop algorithms for removing them from THz-CT reconstructed images, several cylindrically shaped plastic Plexiglas rods (real refractive index 1.54) are used as target material. Cylindrically shaped plastic rods provide a uniform, homogeneous material for development of boundary correction algorithms. Four identical plastic rods were chosen for the study. One of them was kept intact. In two of the samples, a uniform cylindrical shape hole (1mm and 5mm diameter) is drilled near the geometric center of the cylinder. In the fourth sample, a cylindrically shaped hole (5mm diameter) is drilled near the periphery of the sample. These sample plastic rods are subjected to transmission scans by the pulsed THz beam.

The Plexiglas rod and natural cork samples are scanned in transmission using a Picometrix T-Ray 2000 system. Details of the experimental set-up have been discussed in our previous work. [15] For the tomographic scanning, samples are attached to a rotation stage such that the geometric center of the cylinder is nominally collinear with the rotation axis of the stage. Each sample is rotated in 2 degree intervals from zero to 360 degree (up to 180 rotations) relative to its original position. Full tomographic scanning is obtained by vertically (resolution 1mm) and horizontally (0.5mm resolution) scanning a sample at each rotational position.

From the THz time-domain spectra, we calculate the average attenuation (A=ln(1/t)), where T is the transmission at 0.15 THz for each scan position. For each horizontal slice through circular cross-section of the cylinder at a fixed rotational angle, the array of attenuation data represents a projection [3] through the sample. A typical projection for a solid Plexiglas rod is shown in Fig. 1 (a). By measuring the project array at each rotation angle, a 2D reconstruction of the slice can be generated using MATLAB's built in function for Radon transformation with filtered-back propagation. A typical reconstructed slice using the measured (uncorrected) projection arrays is shown in Fig. 1(b). A complete 3D reconstruction is achieved by stacking the reconstructed slices at each vertical position.

Fig. 1 (a) shows a typical plot of the experimentally measured and ideal attenuation projection through a solid Plexiglas rod measured at 0.15 THz. The ideal projection data is calculated using measured values for the real refractive index and the attenuation coefficient

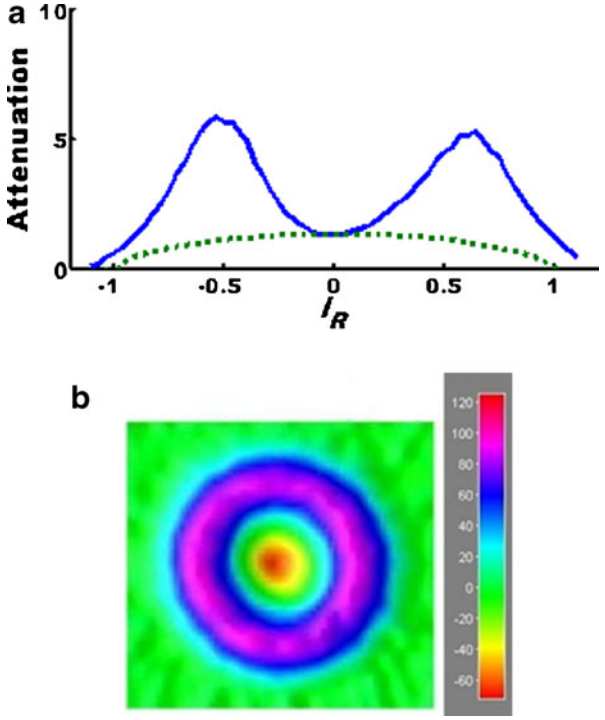

Fig. 1 (Color online) (a) Plot of experimentally measured average THz attenuation (solid) between 0.1-0.2 THz and theoretically calculated attenuation (dashed) of a solid, uniform Plexiglas rod. (b) Reconstructed pulsed THz-CT image of a horizontal slice through a uniform Plexiglas rod

of a homogenous sample. These values can be measured by propagating the THz beam through the diameter of the sample and analyzing the resulting frequency dependent phase and magnitude. The ideal projection assumes that the THz beam propagates straight through the sample. For this ideal projection, the attenuation should depend only on the material's attenuation coefficient α_o and the path length through the sample. The path through the sample depends on the offset distance l relative to the geometric center of the circular cross-section

$$A_{th}(l_R) = \alpha_o L(l_R) = \alpha_o 2R\sqrt{1-l_R^2} \tag{1}$$

where $l_R=l/R$, and R is the radius of the sample. According to Eq. (1), the centre position corresponding to $l_R=0$ should exhibit the maximum attenuation with decreasing attenuation as the offset parameter increases away from the centre diameter. However, in reality, the measured attenuation (Fig. 1(a)) is a minimum at the centre position and increases with increasing $|l_R|$. Consequently, the reconstructed 2D tomographic image of a horizontal slice through the rod shows an enhanced attenuation at the boundaries of the rod (Fig 1(b)). Ideally, the reconstructed attenuation coefficient should be uniform throughout the material.

3 Theoretical Formulation – Fresnel losses

In this work, an algorithm is developed that eliminates the effect of the Fresnel reflection and beam steering, so that the anomalous attenuation shown in the reconstructed image (Fig. 1(b)) can be removed. Essentially the goal is to develop algorithms to correct the measured attenuation curve of (Fig. 1(a)) by removing the effects of Fresnel reflection and beam steering from attenuation projection data prior to reconstructing the image using Radon transformations.

3.1 Fresnel reflection losses

Fig. 2 shows a pictorial depiction of THz beam transmitting through circular cross section of a cylindrical rod. From Fig. 2, the distance that the THz beam travels inside the material upon refraction clearly is not the same as if the beam were to travel in a straight line. Using

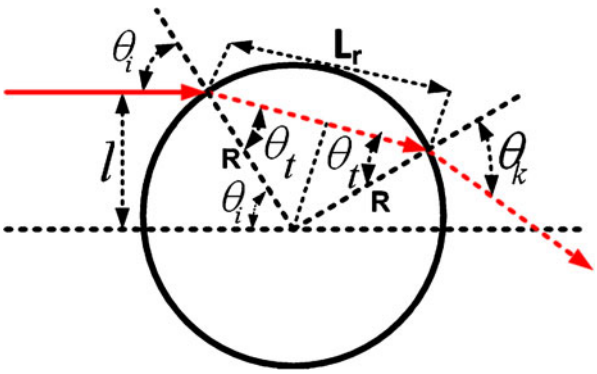

Fig. 2 Transmission of THz beam with bending inside the material

the geometry of Fig. 2 with Snell's law of refraction $n_a \sin\theta_i = n_p \sin\theta_t$, where θ_i and θ_t are the angles of the incident and refracted rays, it is straight forward to show that the path length which the THz beam travels inside of the sample upon refraction is $L_r = 2R\sqrt{1-n_a^2 l_R^2/n_p^2}$, where n_a and n_p are refractive index of air and plastic, respectively. In order to estimate the relative change in length, consider the refractive indices of the plexiglass (1.54) and air (1.0). If the ray were to travel at a distance l_R=1/2 from the centre axis, then the path length through the sample assuming that there is no refraction would be L=1.73R, while the path length with refraction would be L_r=1.89R corresponding to a ~9% increase in path length due to refraction.

For our experimental configuration, the polarization of the incident THz wave is parallel to the plane of incidence. The Fresnel reflection losses can be included using the power reflection coefficient [25]

$$R = \left(\frac{n_t\cos\theta_i - n_i\cos\theta_t}{n_i\cos\theta_t + n_t\cos\theta_i}\right)^2. \tag{2}$$

where n_i, n_t, θ_i and θ_t are refractive index of the incident medium, refractive index of the transmitted medium, incidence and transmitted angle, respectively. Applying both Snell's law and Eq. (2) to both the air-plastic and plastic-air interfaces gives the following reflection losses at the two boundaries

$$R_{ap}(l_R) = \left(\frac{n_p\sqrt{1-l_R^2} - n_a\sqrt{1-n_a^2 l_R^2/n_p^2}}{n_a\sqrt{1-n_a^2 l_R^2/n_p^2} + n_p\sqrt{1-l_R^2}}\right)^2 \tag{3}$$

$$R_{pa}(l_R) = \left(\frac{n_a\sqrt{1-l_R^2 n_a^2/n_p^2} - n_p\sqrt{1-l_R^2}}{n_p\sqrt{1-l_R^2} + n_a\sqrt{1-l_R^2 n_a^2/n_p^2}}\right)^2. \tag{4}$$

The total transmission of a THz beam through the sample can be written as

$$T(l_R) = \left(1-R_{ap}\right)\exp(-\alpha L_r)\left(1-R_{pa}\right) \tag{5}$$

where α is the power attenuation coefficient for the plastic. The first term of Eq. (5) represents the power loss when the THz beam refracts as it enters the sample. The second term represents the attenuation loss of the THz beam propagating through the sample, while the third term represents the reflective power loss as the beam exits the sample. It should be noted that this loss term could be 100% if the THz beam were totally internally reflected at the plastic-air interface. As an estimate of the Frensel power losses, consider a beam travelling through the material at a distance l_R=1/2. Using the measured linear attenuation coefficient α=0.0311/mm and radius of the plastic rod (14mm), the transmission of the THz beam through the material can be estimated from Eq. (5) to be 0.41 including Fresnel reflection losses and roughly 0.47 when the losses are neglected. Therefore, inclusion of the Fresnel losses reduces the transmission by ~14% which corresponds to an attenuation change of about 0.14.

3.2 Beam Steering Losses

While the increase in sample path length and Fresnel losses increase the attenuation from what one would ideally expect for an undeviated beam, the magnitude of these losses is too small to explain the rapid increase in attenuation observed (in Fig 1(a)) as the offset parameter l_R (in Fig. 2) of the THz beam relative to the geometric center of the cylindrical rod is increased. In the absence of the sample, the lenses and other optical components of the THz system are aligned to optimize the THz power from the THz transmitter to the detector. Clearly, the presence of any sample in the beam path becomes part of the optical system since refraction of the THz beam by the sample will steer the THz beam from its optimal path to the detector. As illustrated in Fig. 3 (b), when the cylindrical sample is off center in the THz optical system, the resulting beam steering will reduce the measured THz transmission.

In order to predict the effects of beam steering on the THz-CT system, a ray-tracing software program BEAM4 (https://www.stellarsoftware.com) is used to model the optical system. A table of the optical components, their spatial locations, and physical sizes which were used for the ray-tracing calculation are listed in Table 1 and illustrated in Fig. 3. Using

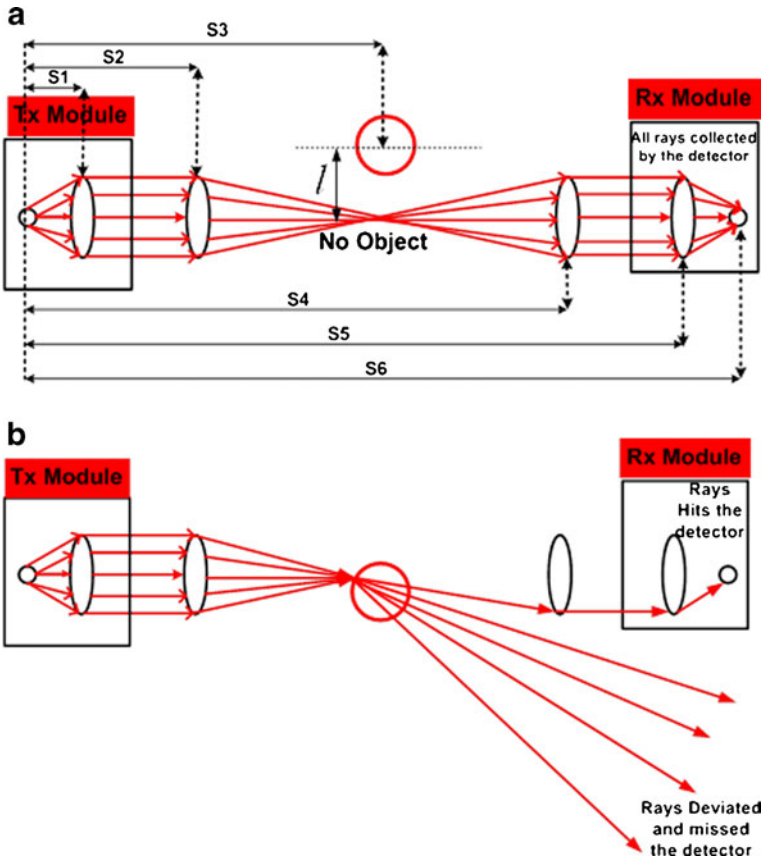

Fig. 3 (a) Illustration of optimal propagation of the THz radiation through the collimating and focusing lenses in the absence of a sample. (b) Illustation of the beam steering of the THz radiation by the sample as an optical component in the system. Tx and Rx stands for transmitter and receiver, respectively

Table 1 Optical components, their locations and physical size used in the experiment

Components	Distance from the source (mm)	Diameter (mm)	Refractive Index	Curvature of the Surface
Source	0	0.1		
First Lens	S1=76.2	38.5	1.5	0.05194/mm
Second Lens	S2=215.1	38.5	1.5	0.05194/mm
Scanned Object	S3=292.1	28	1.1	0.07142/mm
Third Lens	S4=368.3	38.5	1.5	0.05194/mm
Forth Lens	S5=571.5	38.5	1.5	0.05194/mm
Detector	S6=647.7	0.1		

the geometric ray tracing software, we define a fan of rays emerging from the source and trace their progression through the optical components. The fan of rays simulates the THz beam as it propagates through the optical system. By counting the percentage of the rays which propagate through the optical system to the detector as a function of the offset parameter l_R, we estimate the transmission T_{st} of THz radiation. It is assumed that when $l_R = 0$, corresponding to optimal optical alignment, the transmission is a maximum (100%).

The simulated attenuation due to beam steering $A_{st}(l_R) = -\ln(T_{st}(l_R))$ is shown in Fig. 4. For $|l_R|>1$ (2R=28 mm), the attenuation is zero since the sample is not in the path of the THz beam. Note that as $|l_R|$ increases above zero, the predicted attenuation due to beam steering $A_{st}(l_R)$ continues to increase monotonically. In theory, the attenuation due to steering becomes infinite for large values of $|l_R|$ due to extreme beam deviations as well as total-internal reflection of the THz beam at the sample-air exiting interface. In practice, the maximum correctable attenuation should be capped at roughly 4.6 because this is the typical maximum attenuation which can be measured due to the signal-to-noise limitations of our THz spectroscopy system.

In order to define a correction term due to beam steering, we fit the simulated attenuation to a quadratic polynomial given by $\ln(T_{st}(l_R))=al_R^2+bl_R+c$ where a, b, and c are constants determined by the best fit to the data of Fig. 4. Clearly, the fitting parameters will change depending on the refractive index of the smaple. Fitting of the data from Fig. 4 to higher order polynomials (4th order, 6th order and 8th order polynomials) exhibits an improved fit as indicated by lower

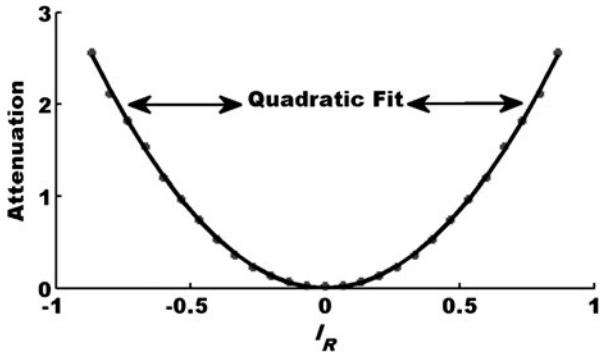

Fig. 4 Predicted attenuation from ray-tracing simulation data (dotted grey curve) and quadratic fit (solid black curve). The fit is determined by - $\ln(T_{st}(l_R))=al_R^2+bl_R+c$ where a is 2.94. The values for b and c are on the order of 10^{-16} and can be regarded as zero respectively

χ^2 values. But when the higher order polynomial fits are used as part of the correction algorithm, the corrected data for a homogenous, uniform plastic rod does not follow the ideal curve of Eq.(1). On the contrary, a quadratic ray-tracing correct term accurately reproduces Eq.(1). For this reason a quadratic polynomial has been used to fit the ray-tracing correction curve.

The effects of beam steering can be included into Eq. (5). Using an additional factor T_{st} (l_R) which accounts for the effective transmission of the THz-CT system in the presence of beam steering

$$T(l_R) = T_{st}(l_R)\exp(\alpha L_r)\left(1-R_{pa}\right)\left(1-R_{ap}\right) \tag{6}$$

where the left-hand side of Eq. (6) is the measured THz transmission. Solving this equation for the parameter of interest αL_r gives

$$\alpha L_r = -\ln(T(l_R)) + \ln(T_{st}(l_R)) + \ln\left(1-R_{pa}\right) + \ln\left(1-R_{ap}\right). \tag{7}$$

Equation (7) illustrates the three correction terms which are applied to the measured THz attenuation prior to reconstructing the THz-CT image using a Radon transformation. The αL_r term represents the corrected attenuation projection array data which will be inverted using the Radon transformation. The $-\ln(T(l_R))$ term is the experimentally measured attenuation. The $\ln(T_{st}(l_R))$ term is the correction for beam steering, while the $\ln(1-R_{pa})$ and $\ln(1-R_{ap})$ terms account for the Fresnel's reflection loss at the incident and exiting air-plastic interfaces.

3.3 Corrections for Finite Beam Size

The shape of the measured attenuation near the sample boundaries results from the finite beam size of the probing THz beam. For large values of $|l_R| > 1.11$, the sample is not in the THz beam path and the measured THz transmission (attenuation) is unity (zero). As the sample is scanned horizontally in l_R, the edge of the sample partially blocks the THz beam leading to an increase in measured attenuation. Due to the large angle of incidence near the edges of the sample, the beam steering is so severe as none of the light which enters the sample is able to propagate to the detector. The attenuation near the edges of the sample, therefore, can be modelled assuming that the edge of the sample partially blocks the THz beam. Assuming that the THz beam propagates in the z direction as a Gaussian beam with a spot size of a_o at the focus, the local intensity of the THz beam is given by [26]

$$I(x,y) = I_o\exp\left(-2\left(x^2+y^2\right)/a_o^2\right) \tag{8}$$

where $I_0 = \frac{2P_0}{\pi a_0^2}$ and P_0 is the total power of the beam at any cross section. The total power of THz radiation which gets blocked by the sample edge can be calculated by integrating Eq. (8) over the transverse directions as illustrated in Fig. 5.

The measured transmittance near the sample's right edge (corresponding to positive values of l_R) should be

$$T_{edge}(l_R) = \sqrt{\frac{2}{\pi}}\frac{1}{a_0}\int_{-R(l_R-1)}^{\infty}\exp\left(-2x^2/a_0^2\right)dx \tag{9}$$

where l_R respresents the horizontal (ie. x) location of the sample's edge from the centre of the beam. After integrating Eq. (9) and taking the negative of natural log on the right side of the expression, one can derive the attenuation near the sample right edge as,

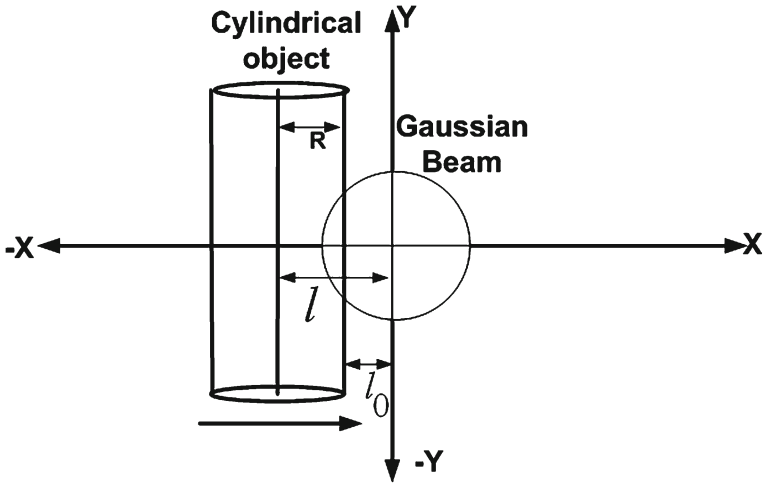

Fig. 5 A cyllindrical object approaching a Gaussian beam which is propagating perpendicular to the page

$$A_{edge}(l_R) = -\log_e\left[\frac{1}{2} + \frac{1}{2}erf\left(\frac{\sqrt{2R}}{a_0}(l_R - 1)\right)\right] \tag{10}$$

For the left edge (negative values of l_R), the equation is the same except the limits of integration range from negative infinity to $-R(l_R + 1)$.

Fig. 6 (a) shows a comparison of the measured THz attenuation $-\ln[T(l_R)]$ with beam steering correction term $-\ln[T_{st}(l_R)]$. The correction term has been offset vertically in the plot in order to compare the shapes of the two curves. Note that the similarity in the two curves strongly suggests that the large increase in attenuation with increasing offset parameter l_R is primarily due to beam steering. In Fig. 6(a), we show a typical plot of Eq. (10) for the left and right edges. From a best fit to the experimental data, we extract the fixed THz beam spot size (a_0=2mm) as well as the values of l_R for the left and right edges of the sample. The l_R position of the sample's physical edge is determined when the measured value for the attenuation $A_{edge}(l_R) = \ln(2)$ corresponding to half of the THz beam being blocked by the sample's edge.

As part of the correction algorithm, one must account for the fact that the rotational axis for the tomography scans does not exactly coincide with the geometric axis of the cylindrical rod. Consequently, the first step in the correction algorithm is to use Eq. (10) to determine the left and right boundaries of the rod. Once these boundaries are determined, the offset between the rotational and geometric axes can be used to apply correction terms of Eq. (6) for both Fresnel reflection losses and beam steering.

While the beam steering and Fresnel correction factors of Eq. (6) can be used to correct the middle portion of the projection data, the THz-TDS system's detection limit as well as the severe beam steering when the THz beam passes near the edges of the rod implies that the measured attenuation for $|l_R| > 0.36$ in Fig. 6(a) is an artifact and not related to the attenuation of the sample material. Near the edge of the sample, the deviation of the THz beam is so large that much of the beam from that region does not reach the detector. Since THz radiation which passes through this region is not detected, tomographic information from this region can not be determined and thus we call that area a 'blind' region. In order to correct the attenuation projection data

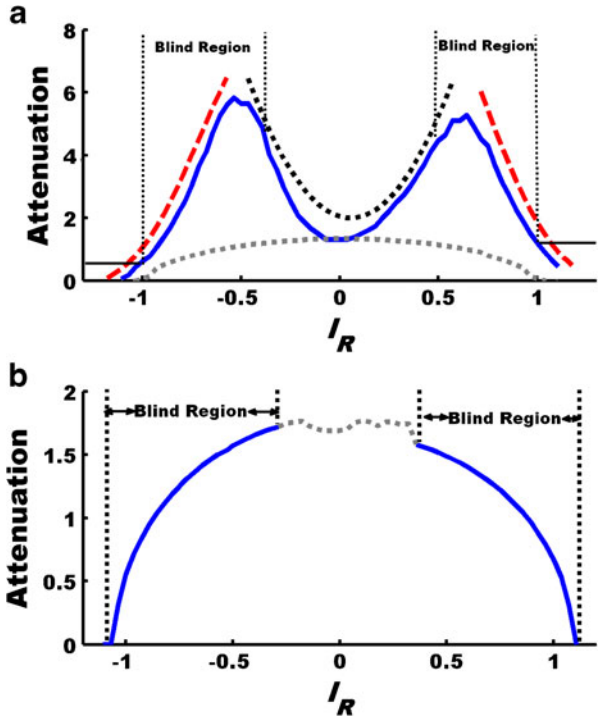

Fig. 6 (a) Plot of experimentally measured attenuation (solid line), the ideal attenuation projection (gray dotted line) assuming no refraction, beam steering correction (dotted line) and predicted attenuation due the samples edge blocking the THz beam (dashed line). (b) Corrected attenuation from Eq. (7) using the beam steering correction term determined from ray-tracing and Eq. (10) to determine the edges of the sample

near the blind region of the sample, one must assume a functional form for the data in this range and match the experimental data to the measured values in the regions which are valid. Since the cylindrical rods are supposed to be homogenous and uniform, the expected functional form for the attenuation project array should ideally (in the absence of refraction) be due only to the attenuation coefficient α_o of the material and the length of material through which the THz beam propagates.

At the physical edge corresponding to $l_R = 1$, the attenuation through the material should have a limiting value of zero. Since the radius of the rod is known, the only free parameter in Eq. (1) is the attenuation coefficient α_o. This value is determined by matching the attenuation value from Eq. (1) to the corrected value of the measured attenuation from Eq. (7) at a fixed value of l_R corresponding to the attenuation detection limit of the THz-TDS system. As an example, Fig. 6(b) shows the corrected attenuation projection data for a fixed rotation angle and illustrates regions of experimentally corrected attenuation as well as regions near the periphery of the sample for which the attenuation is assumed to follow Eq. (1).

In summary, the correction algorithm is applied as follows:

- For each projection slice, use Eq. (10) to determine the location of the left and right edges of the cylinder relative to the center of rotation of the sample.
- Based on the maximum detectable attenuation (typically ~4.6) , determine the range of l_R values for which the measured attenuation is not instrument limited.
- Apply the correction terms of Eq. (7) to that range of l_R parameters

- Use the ideal form for the attenuation Eq. (1) to fill in projection array data as a function of l_R in the 'blind' region from the sample's edges to the boundary of the valid corrected data.
- Repeat for each projection slice for all rotation angles of the sample.

4 Results and Discussions

The correction algorithm described in Section 3 is applied to all of the projection data as a function of sample rotation from the homogenous plexiglass rod and the results are shown in Fig. 7. Comparing the reconstructed image with (Fig. 7 (a)) and without (Fig. 1 (b)) correction clearly shows that the anomolously large attenuation near the boundaries of the rod have been removed in the reconstructed image. Fig. 7(b) shows a profile of the reconstructed localized attenuation coefficient taken along a diameter through Fig. 7 (a). Note that the localized attenuation coefficent is nearly constant across the sample as would be expected for a homogeneous sample.

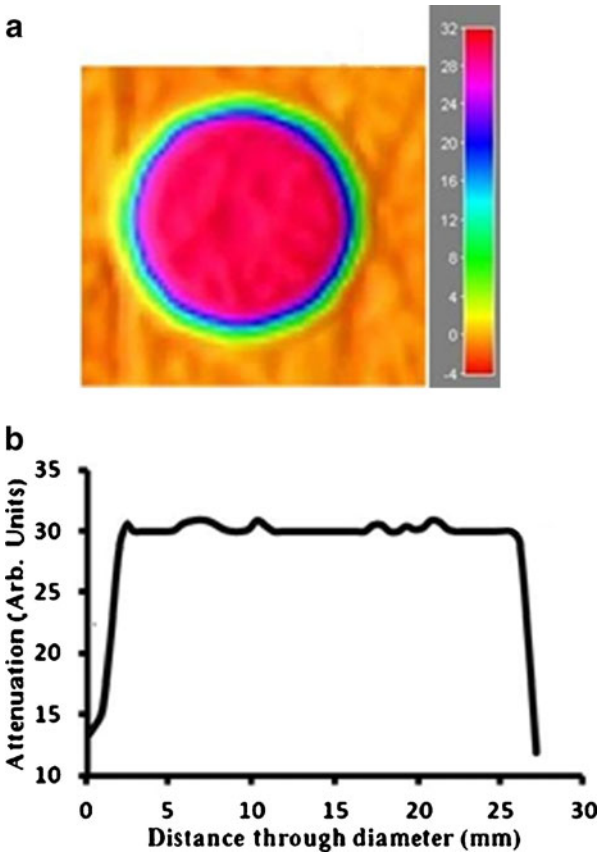

Fig. 7 (a) Reconstructed pulsed THz-CT image of a circular cross-section through homogeneous cylindrical Plexiglas rod after correction algorithm is applied to the measured projection data. (b) Plot profile of through a diameter of (a). Note the contrast bewteen the corrected images and the uncorrected image of Fig. 1b

Clearly, THz rays which pass near the boundary of the object are subjected to severe beam steering. For a homogenous material for which Eq. (1) is a good representation of the true sample attenuation, there is not much error in the reconstructed image by using Eq. (1) to match the projection array data from the physical edge of the sample to the regions for the measured attenuation is accurately measured. However, if a structural feature were present in the peripheral region of the sample, the measured attenuation – since it is dominated by the blocking of the THz beam by the sample's edge – would not be representative of the structure feature. In essence, the measured THz attenuation near the periphery of the sample is 'blind' to the presence of any structural features which might cause either an increase or decrease in the measured attenuation. For the blind regions, no real information about the internal structure of the object can be obtained.

In order to test the sensitivity of the algorithms of Section 3 to the presence of defects near the periphery of a sample, the algorithms were applied to three plastic rods with defects as discussed in Section 2. The reconstructed images of the rod with 1 mm hole near the centre are shown both without (Fig. 8 (a)) and with application of the correction algorithm (Fig. 8 (b)). The reconstructed local aborbance along slices through the images are shown in Fig. 8 (c) and Fig. 8 (d). The reconstructed hole appears as a spot of large localized attenuation because the hole itself acts as a beam steering obstruction which deviates the THz rays resulting in an increased of attenuation. The reconstructed hole size appears larger than the actual size of the hole which we attribute to the finite size a_0 = 2 mm of the THz beam.

Fig. 9 shows the 2D THz-CT reconstructed images and plot profiles of a plastic rod with a 5mm hole near the center region. Without correcting for the boundary effects, note that the

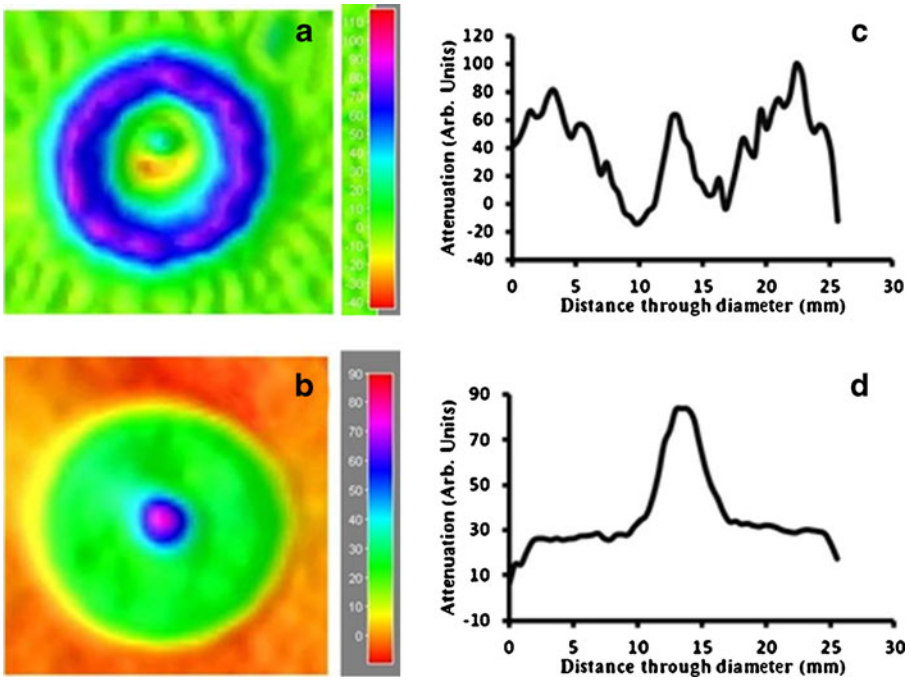

Fig. 8 Reonstructed 2D tomographic images of the plastic rod with a 1mm hole near the centre without (a) and with (b) correction algorithm applied. Corresponding plot profile of the images taken through the diameters are indicated in (c) no correction applied and (d) correction applied

presence of the 5mm hole in the reconstructed image (Fig. 9 (a)) is not as prominent as when the correction algorithms are applied. After correction, both the shape and approximate size of the defect are reconstructed in Fig. 9(b) and Fig. 9(d). In both Fig. 8 and Fig. 9, the hole in the rod steers the THz from its nominal direction leading to an increase in measured attenuation. Clearly, the increase in attenuation due to the presence of the hole is much more prominate when the boundary effects are eliminated using the correction algorithms. These results suggest that the application of the correction algorithms should work reasonably well if any defects are in the central region of the plastic rods.

However, when the defect in the rods is located in the 'blind' region near the physical boundaries of the rod, discerning the hole near the edge becomes difficult. Fig. 10 shows the 2D reconstructed images and plot profiles of a plastic rod having a 5mm diameter hole near to the edge of the rod. In comparing Fig. 10(a) with Fig. 1(b), it is clear that the distortion of the uncorrected reconstructed image near the top edge of the rod corresponds to a defect in the material, but the shape of the defect is unrecognizable. When the correction algorithm is applied, the resulting reconstructed image does show the presence of a defect in the material (comparing Fig. 10(b) with Fig. 8(a), but neither the shape nor the exact location of the defect is accurately determined. The source of the error can be understood to result from incorrect

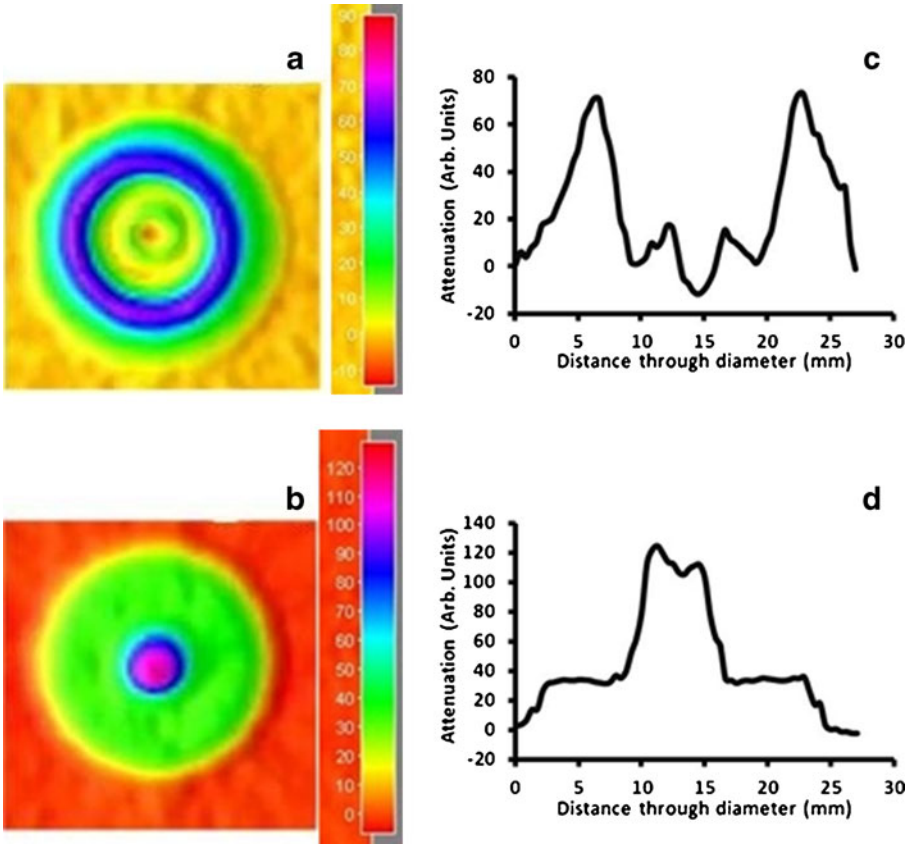

Fig. 9 Reconstructed 2D tomographic images of the plastic rod with a 5mm hole near the centre with (a) and without (b) correction algorithm applied. Corresponding plot profile of the images taken through the diameters are indicated in (c) no correction applied and (d) correction applied

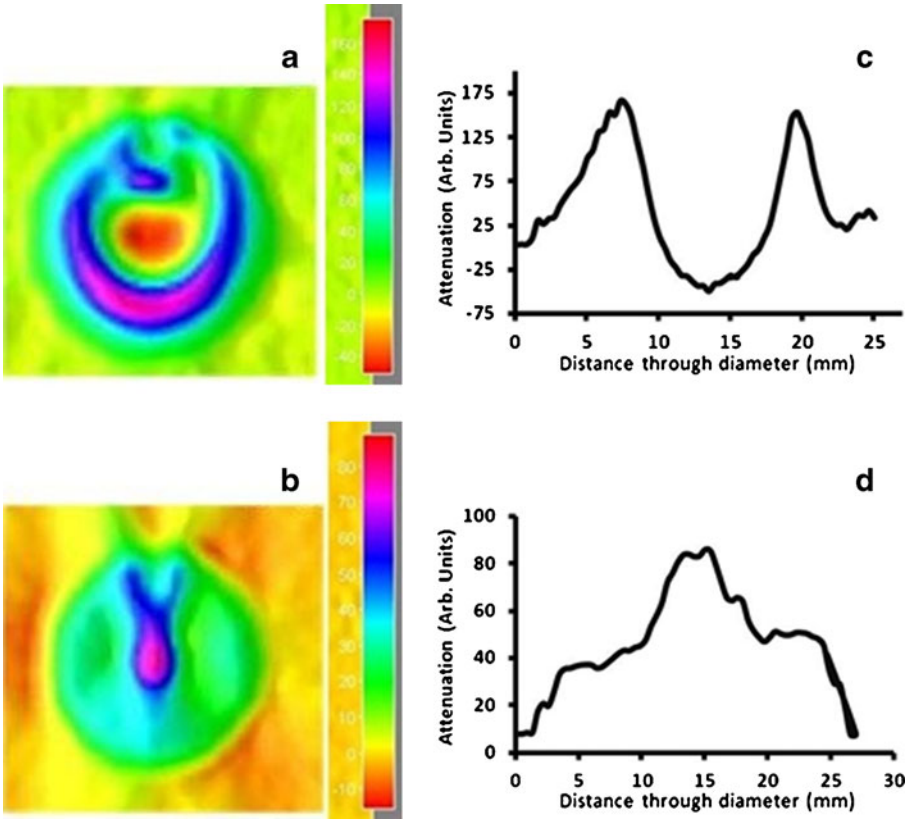

Fig. 10 Reconstructed 2D tomographic images of the plastic rod with a 5mm hole near the periferry of the sample without (a) and with (b) correction algorithm applied. Corresponding plot profile of the images taken parallel to the bottom of the page through the diameters are indicated in (c) with no correction applied and (d) correction applied

projection data as a function of sample rotation. For a certain range of rotation angles, the hole near the periphery of the sample is in a 'blind' spot. For other angles, the probing THz radiation will interact with the hole and manifest the presence of the hole through an increase in the measured attenuation. The presence of the hole in attenuation projection data for some but not all of the rotation angles leads to errors in the reconstructed image.

As an example of a potential application, we apply the correction algorithms to attenuation projection data from natural cork wine stoppers. For this material, the presence of lenticel structures as well as internal cracks and voids are characterized by an increase in the measured THz attenuation [14]. Lenticels are naturally occurring cell structures which enable the exchange of gases between the atmosphere and the interior of plant tissues. While an accurate reconstruction of an object with arbitrary shape and composition by THz CT is problematic due to refraction artifacts, THz CT can still be an effective NDE tool for corks since the size and shape of cork stoppers are standardized. Moreover, the relatively low refractive index (approximately 1.1) of natural cork reduces both the refractive and beam steering effects and the volume of 'blind' volumes within the cork relative to the Plexiglas samples discussed above. Removing the boundary artifacts enables a more detailed reconstruction of each sample's internal structure which is so critical to the functionary of the stoppers with regards to their gas and liquid diffusion properties [16, 27].

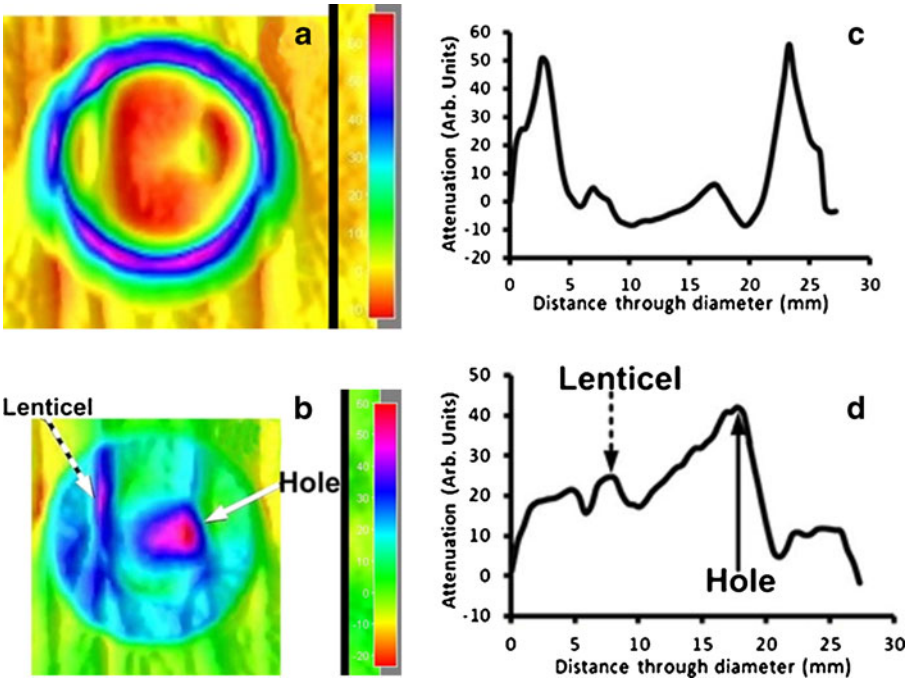

Fig. 11 Reconstructed 2D tomographic images of the natural cork without (a) and with (b) correction algorithm applied. The round spot near the solid arrow is an insect hole in the cork while the dashed arrow indicates a lenticular channel in the cork structure. Corresponding plot profile of the images taken parallel to the bottom of the page through the diameters are indicated in (c) with no correction applied and (d) correction applied

To test the correction algorithms on a cylindrically shaped natural cork stopper, we select a cork sample with a ~3mm diameter hole which was bored into the sample by an insect. This insect hole is analogous to the holes which were drilled into the plastic rod samples. Fig. 11 shows the 2D reconstructed THz-CT images of the cork sample. Since cork has a lower refractive index than plastic, the bending and steering of the THz beam is much less inside the cork than inside the plastic. Without application of the correction algorithms, Fig. 11 (a) shows a prominent boundary surrounding the cork. However, when the correction algorithm is applied (Fig. 11 (b)), the boundary is removed and more of the cork's internal structure is revealed. The arrows in Fig. 11 (b) illustrates the location of the insect hole and lenticel channel in the cork which is not visible in Fig. 11 (a). Plots of the reconstructed attenuation through the diameter of the cork (Fig. 11 (c) and Fig. 11 (d)) illustrates that the correction algorithms remove the boundary artifact and enable visualization of the sample's internal structure.

5 Conclusion

Due to the finite beam size of the probing THz radiation as well as strong refractive effects in the THz range including refractive power losses and beam steering, artificially large boundaries are produced in reconstructed THz-CT images. Of these three effects, the beam steering is found to introduce the largest distortion in the THz projection data. In this paper, a correction algorithm is introduced for cylindrically shaped objects which can be applied to the projection array data prior to reconstruction of the THz-CT image using Radon

transformations. The algorithm corrects the edges of the projection data for the finite THz beam size as well as beam steering and Fresnel reflection losses. When the algorithms are applied to plastic rods, the artifically large attenuation near the boundary of the cylindrical sample is removed. Defects such as holes which are present near the central region of the sample are reproduced using the correction algorithms. When the defects are located near the periphery of the sample, the correction algorithms indicate the presence of the defect, but can not accurately determine the shape nor exact location of the defect. When the correction algorithms are applied to a low refractive index (~1.1) material such as natural cork, the boundary effect is significantly reduced in the reconstructed images enabling visualization of the cork's internal structure including holes and lenticels.

Acknowledgement This work was partially supported by the European Science Foundation.

References

1. B.B.Hu and M.C.Nuss, Optics Letters. 20(16): pp. 1716–1718 (1995).
2. D.Mittleman, IEEE Journal of selected optics in quantum electronics, 2(3): pp. 679–692 (1996).
3. S.Wang and X-C Zhang, Journal of Physics D, 37(4): pp. R1-R36 (2004).
4. D.Mittleman, S.Hunsche, L.Boivin, and M.C.Nuss, Optics Letters, 22(12): pp. 904–906 (1997).
5. A. Brahm, M. Bauer, T. Hoyer, H. Quast, T. Loeffler, S. Riehemann, G. Notni, and A. Tunnermann, Infrared, Millimeter and Terahertz Waves (IRMMW-THz), 2011 36th International Conference: (2011).
6. T. Buma and T.B. Norris, Applied Physics Letters, 84(12): pp. 2196–2198 (2004).
7. W. Sun, X. Wanl, Y. Cui, and Y. Zhang, The European Conference on Lasers and Electro-Optics, Munich, Germany: (2011).
8. Li.Qi, Li.Yun-Da, D.Sheng-Hui, and W.Qi, Journal of Infrared, Millimeter, and Terahertz Waves, **33**(5): pp. 548–558 (2012).
9. A.Wei-Min-Lee, K.Tsung-Yu, D.Burghoff, Q.Hu, and J-.Reno, Opt. Lett., 37(2): pp. 217-219(2012).
10. B.Ferguson, S.Wang, D.Gray, D.Abbot, and X-C.Zhang, Optics Letters, 27(15): pp. 1312–1314 (2002).
11. M.Bessou, B.Chassagne, J-P.Caumes, C.Pradère, P.Maire, M.Tondusson, and E.Abraham, Appl. Opt., 51(28): pp. 6738–6744 (2012).
12. D.J.Roth, S.B.Reyes-Rodriguez, D.A.Zimdars, R.W.Rauser, and W.W.Ussery, 69(9): Materials Evaluation, pp. 1090–1098 (2011).
13. B.Recur, A.Younus, S.Salort, P.Mounai, B.Chassagne, P.Desbarats, J-P.Caumes, and E.Abraham, Optics Express, 19(6): pp. 5105–5117 (2011).
14. Y.Hor, J.F.Federici, and R.L. Wample, Applied Optics, 2008. 47: pp. 72–78.
15. S.Mukherjee and J.F.Federici, IRMMW-THz 2011 - 36th International Conference on Infrared, Millimeter, and Terahertz Waves, Houston, Texas, USA: p. 85 (2011).
16. A. J. Teti, D. E. Rodriguez, J. F. Federici, and C. Brisson, J. Infrared Milli. Terahz. Waves, 32: pp. 513–527 (2011).
17. J.F. Federici, Journal of Infrared, Millimeter and Terahertz Waves, 33(2): pp. 97–126 (2012).
18. B.Ferguson, S.Wang, D.Gray, D.Abbott, and X-C.Zhang, Physics in Medicine and Biology, 47(21): pp. 3735–3742 (2002).
19. X-C.Zhang, Philosophical Transactions of The Royal Society A, 362: pp. 283–299 (2003).
20. W.L. Chan, J. Deibel, and D.M. Mittleman, Reports on Progress in Physics, 70(8): pp. 1325–1379 (2007).
21. K.Hyeongmun, K.Kyung-Won, S.Joo-Hiuk, and H.Joon-Koo, Optical Society of America (2012).
22. S.A.Nishina, K.A.Takeuchi, M.A.Shinohara, M.A.Imamura, M.B.Shibata, Y.B.Hashimoto, and F.B.Watanabe, SAE International Journal of Fuels and Lubricants, 5(1): pp. 343–351 (2012).
23. B. Recur, J. P. Guillet, I. Manek- onninger, J. C. Delagnes, W. Benharbone, P. Desbarats, J. P. Domenger, L. Canioni, and P. Mounaix, Optics Express, 20(6): pp. 5817–5829 (2012).
24. E. Abraham, A. Younus, C. Aguerre, P. Desbarats, and P. Mounaix, Optics Communications, 283(10): pp. 2050–2055 (2010).
25. Eugene Hecht, *Optics*, 4th edn, (Addison Wesley, 2001).
26. E. D. Hirleman, and, and W. H. Stevenson, Applied Optics, 17(21): (1978).
27. H. Pereira, *Cork: Biology, Production and Uses*, (New York: Elsevier. 2007).